ARTICLE

Check for updates

Pair suppression caused by mosaic-twist defects in superconducting Sr_2RuO_4 thin-films prepared using pulsed laser deposition

Carla Maria Palomares Garcia [1], Angelo Di Bernardo [1], Graham Kimbell [1], Mary E. Vickers[1], Fabien C-P. Massabuau[1,2], Sachio Komori[1], Giorgio Divitini [1], Yuuki Yasui [3], Han Gyeol Lee[4,5], Jinkwon Kim[4,5], Bongju Kim[4,5], Mark G. Blamire [1], Antonio Vecchione[6], Rosalba Fittipaldi[6], Yoshiteru Maeno[3], Tae Won Noh [4,5] & Jason W. A. Robinson [1✉]

Sr_2RuO_4 (SRO_{214}) is a prototypical unconventional superconductor. However, since the discovery of its superconductivity a quarter of a century ago, the symmetry of the bulk and surface superconducting states in single crystal SRO_{214} remains controversial. Solving this problem is massively impeded by the fact that superconducting SRO_{214} is extremely challenging to achieve in thin-films as structural defects and impurities sensitively annihilate superconductivity. Here we report a protocol for the reliable growth of superconducting SRO_{214} thin-films by pulsed laser deposition and identify universal materials properties that are destructive to the superconducting state. We demonstrate that careful control of the starting material is essential in order to achieve superconductivity and use a single crystal target of $Sr_3Ru_2O_7$ (SRO_{327}). By systematically varying the SRO_{214} film thickness, we identify mosaic twist as the key in-plane defect that suppresses superconductivity. The results are central to the development of unconventional superconductivity.

[1] Department of Materials Science & Metallurgy, University of Cambridge, 27 Charles Babbage Road, Cambridge, United Kingdom. [2] Department of Physics, SUPA, University of Strathclyde, Strathclyde, United Kingdom. [3] Department of Physics, Graduate School of Science, Kyoto University, Kyoto 606-8502, Japan. [4] Center for Correlated Electron Systems, Institute for Basic Science (IBS), Seoul 08826, Republic of Korea. [5] Department of Physics and Astronomy, Seoul National University, Seoul 08826, Republic of Korea. [6] Consiglio Nazionale delle Ricerche, SPIN, Via G. Paolo II 132, I-84084 Fisciano, Italy. ✉email: jjr33@cam.ac.uk

The past decade has seen rapid developments in the understanding of unconventional superconductivity, particularly in proximity-coupled systems involving conventional s-wave superconductors in combination with magnetic materials and interfaces with strong spin-orbit coupling[1]. Highlights include the discovery of odd-frequency (s-wave) spin-triplet pairing at s-wave superconductor/ferromagnet interfaces[2–10], evidence for electron-composite particle-antiparticles in nanowire devices with spin-orbit coupling and superconductivity[11,12], and surface superconductivity in Au with Fermi-level tuning via a ferromagnetic dielectric[13].

Parallel research on intrinsic unconventional superconductivity in superfluid He and in compounds such as Sr_2RuO_4 (SRO_{214})[14,15] has also made dramatic advances. Single crystal SRO_{214} has a superconducting critical temperature[16] (T_c) of 1.5 K. Although the underlying nature of the superconducting state in SRO_{214} crystals remains highly controversial, the consensus from experiments and theory is that the pairing is unconventional and potentially chiral p-wave state with the d-vector perpendicular to the basal plane[17], which is even-frequency and conceptually different from the odd-frequency spin-triplet pairing induced at s-wave superconductor/ferromagnetic interfaces. Muon spin-relaxation measurements[18,19] on SRO_{214} show evidence for time-reversal symmetry breaking below T_c while early nuclear magnetic resonance spectroscopy[20,21] and polarized neutron scattering[22] experiments have demonstrated a constant in-plane spin susceptibility (Knight shift) below T_c. However, a constant out-of-plane spin susceptibility below T_c goes against a chiral p-wave state[17]. Furthermore, recent nuclear magnetic resonance spectroscopy on SRO_{214} crystals show that the Knight shift decays in the superconducting state in the "3 K phase" under uniaxial stress as well as in the "1.5 K phase" without stress[23], consistent with a d-wave or helical p-wave state.

Although there is a lack of experimental consistency in the underlying superconducting symmetry of SRO_{214}, unconventional pairing states are expected on the surface due to broken inversion symmetry, which raises the prospect of coupling different superconducting symmetries via proximity effects with s-wave or even d-wave superconductors. Nevertheless, developing a full understanding of the superconductivity in SRO_{214} including proximity-based experiments is fundamentally limited by the fact that thin-film growth of SRO_{214} has proven to be extremely challenging. A robust, reliable, growth protocol for SRO_{214} thin-films is therefore required in order to break the deadlock and enable detailed studies of the electron pairing in SRO_{214} and the mixing of different superconducting symmetries in hybrid Josephson junctions.

One of the key issues for growing superconducting films of SRO_{214} relates to the destructive nature of magnetic or non-magnetic impurities and structural defects. In thin-films, the concentration of impurities and structural defects tends to be high and superconductivity is suppressed or localized to pristine regions[24–27]. Currently, there exist only a few reports of superconducting SRO_{214} thin-films, but control continues to be severely limited because the underlying materials properties required for superconductivity remain poorly understood. The first successful report of a superconducting thin-film of SRO_{214} nearly a decade ago was fabricated by pulsed laser deposition from a stoichiometric (polycrystalline) target of SRO_{214} on (0 0 1) $(La_{0.3}Sr_{0.7})(Al_{0.65}Ta_{0.35})O_3$ (LSAT) single crystals, and required high-temperature layer-by-layer growth[28]. This work was later reproduced by our group[29] in one sample albeit with an extremely broad (1.6 K) superconducting transition and an elevated T_c of 1.9 K. This result indicated inhomogeneous superconductivity due to out-of-plane defects from stacking faults that create local strain, which locally enhances T_c. Recently, superconducting films

of SRO_{214} have been grown by molecular beam epitaxy on LSAT with a T_c of 1.1 K using a Ru-rich flux during growth to reduce Ru loss[30]. The T_c was further enhanced to 1.9 K by depositing onto single terminated (1 1 0) $NdGaO_3$ due to the associated misfit strain[31].

In this article we set out to develop a protocol for the reliable growth of superconducting SRO_{214} thin-films by pulsed laser deposition and to establish and control key materials properties that are destructive for superconductivity. This is achieved using careful control of the starting material, which consists of a single crystal target of $Sr_3Ru_2O_7$ (SRO_{327}). We establish that mosaic twist is a universal structural (in-plane) defect that destroys superconductivity in SRO_{214}. This is clearly different from the planar defects (out-of-phase boundaries) reported by Krockenberger[28]. By controlling the degree of mosaic twist in the SRO_{214} films, and the associated dislocations that form at the SRO_{214}/substrate interface, we demonstrate a reliable protocol for depositing superconducting SRO_{214}.

Results

Growth optimization of SRO_{214} thin films. A single crystal target of SRO_{327} provides 33% Ru excess that compensates for Ru loss during the high-temperature growth of SRO_{214} which, in conjunction with fine-control of laser fluence[32] (see Supplementary Fig. 1 for results using a polycrystalline target of SRO_{214}), reduces the volume fraction of impurity phases present in the films. The single crystal target of SRO_{327} (see compositional analysis in Supplementary Fig. 2a) has a surface area of 3×10 mm^2 and is mounted on a polycrystalline SRO_{214} holder (Fig. 1a). Laser alignment is optimized by focusing the laser spot (1.5 mm diameter) onto the SRO_{214} holder prior to ablating from the SRO_{327} target. During film growth, the rotation of the SRO_{327} target is fixed and the target carousel is twisted through an angle β to erode the SRO_{327} target along a line (Fig. 1b). All SRO_{214} films discussed in this paper are deposited onto heated (950 °C) LSAT (0 0 1) as described in the Methods section. Most of the films are grown using a laser pulse frequency of 2 Hz with one sample grown at 4 Hz as discussed at the end of the paper. To minimise in-plane epitaxial strain, SRO_{214} (in-plane lattice constant = 0.3873 nm) is grown on LSAT (in-plane lattice constant = 0.387 nm) substrates, and a substrate miscut angle of less than 0.05° is used to reduce the concentration of out-of-plane stacking faults at step edges.

We first discuss the effect of varying oxygen pressure (P_{O2}) during growth. SRO_{214} films are grown using a fixed number of laser pulses (5000) at 2 Hz and laser fluence of 1.0 J cm^{-2} to achieve a thickness (t) around 23 nm (depending on P_{O2}). Values of t are estimated by fitting thickness fringes to the (0 0 6) diffraction peak of SRO_{214} (see Supplementary Note 1 and Supplementary Fig. 3). In Fig. 1c we have plotted X-ray diffraction traces from three representative SRO_{214} films grown using 1.0 Pa, 0.35 Pa and 0.09 Pa of oxygen. For the $P_{O2} = 1.0$ Pa film, thickness fringes are barely visible on the (0 0 6)$_{214}$ peak and an SRO_{327} impurity phase is present (highlighted in green). The $P_{O2} = 0.35$ Pa film, however, shows no detectable evidence for SRO_{327} or other impurity phases and the (0 0 6)$_{214}$ peak shows clear fringes, indicating uniform growth. Reducing P_{O2} further to 0.09 Pa promotes secondary phases in the Ruddlesden-Popper series (indicated by magenta) such as SRO_{327}, SRO_{4310} or RuO_2. While thin films deposited above or below $P_{O2} = 0.35$ Pa show metallic behavior with no detectable evidence for superconductivity down to 300 mK, the $P_{O2} = 0.35$ Pa film shows a downturn in $R(T)$ below 0.5 K, consistent with the onset of incipient superconductivity (Supplementary Fig. 4a). The corresponding lattice parameters are $a = 0.3870(3)$ nm (from RSM on (2014)
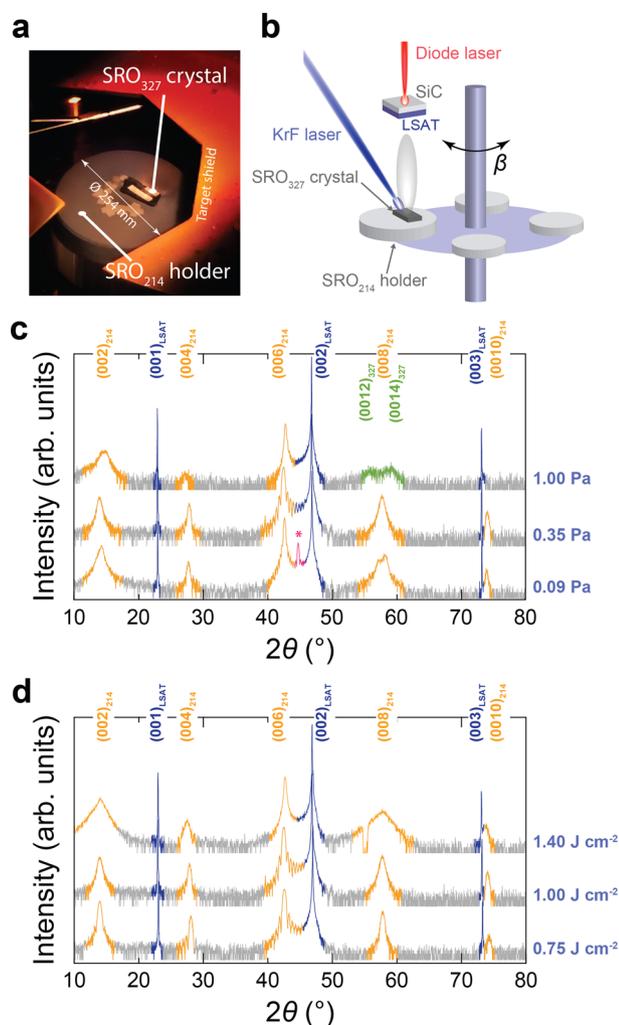
Fig. 1 Pulsed laser deposition setup and structural properties of Sr₂RuO₄ thin films. a A photograph showing a single crystal $Sr_3Ru_2O_7$ target mounted on a polycrystalline Sr_2RuO_4 holder. **b** A schematic illustration of the pulsed laser deposition setup, where the rotation of the target carousel is labelled "β" **c, d** X-ray diffraction traces for Sr_2RuO_4 grown at 950°C under different O_2 pressures (labelled) with a fixed fluence of $1.0\,J\,cm^{-2}$ (**c**) and equivalent traces in which Sr_2RuO_4 is grown at 950°C using different laser fluences (labelled) with a fixed oxygen pressure of 0.35 Pa (**d**). The diffraction planes for Sr_2RuO_4 (orange) SRO_{327} (green), and $(La_{0.3}Sr_{0.7})(Al_{0.65}Ta_{0.35})O_3$ (LSAT) (blue). The peak marked "*" corresponds to the diffraction plane of the Ruddlesden-Popper series (0 0 10)$_{327}$, (0 0 14)$_{4310}$ or (2 1 0) diffraction plane of RuO_2. The subindexes 214, 327 and 4310 refer to Sr_2RuO_4, $Sr_3Ru_2O_7$ and $Sr_4Ru_3O_{10}$, respectively.

plane) and $c = 1.2738(17)$ nm (from a 2θ-ω scan on the (0 0 l) peak positions after applying a correction for sample displacement).

Using $P_{O2} = 0.35$ Pa, we now discuss the effect of laser fluence on the structural and electrical properties of SRO_{214}. In Fig. 1d we have plotted X-ray diffraction traces from three films grown using laser fluences of $0.75\,J\,cm^{-2}$, $1.0\,J\,m^{-2}$ and $1.4\,J\,cm^{-2}$, with a fixed number of laser pulses (5000). The traces show sharper peaks with decreasing laser fluence, indicating improved structural properties (vertical microstrain). The in-plane resistance versus temperature $R(T)$ for the $1.4\,J\,cm^{-2}$ film saturates to a constant minimum below 10 K with no evidence for superconductivity down to 300 mK. In contrast to the $1\,J\,cm^{-2}$ film, the $0.75\,J\,cm^{-2}$ film shows sharper diffraction peaks, but a downturn in $R(T)$ is not observed, even down to 300 mK

(Supplementary Fig. 4b). This is likely due to the lower laser fluence reducing Ru ablation from the SRO_{327} target[32] and hence, the SRO_{214} film is deficient in Ru, which prevents superconducting behaviour[29,30].

Characterization of superconducting properties. We now discuss electrical transport of SRO_{214} films versus t in the 15 nm to 166 nm range using optimized growth parameters (oxygen pressure of 0.35 Pa and fluence of $1.0\,J\,cm^{-2}$). For each film we investigate $R(T)$ and for those that show a superconducting transition, we define T_c as the temperature halfway through the resistive transition. In Fig. 2a we have plotted $T_c(t)$ where the vertical error bars represent the temperature width of the superconducting transition (See Supplementary Fig. 5). These data show a critical thickness for superconductivity of approximately 50 nm with T_c rising to 1.05 K for $t = 166$ nm (Fig. 2a). Although the largest T_c is lower than the T_c of bulk SRO_{214} single crystals (1.5 K[16]), T_c values are higher than previous reports for SRO_{214} films grown by pulsed laser deposition (Supplementary Fig. 6a).

In Fig. 2b we have plotted the t-dependence of the residual resistivity ratio (RRR), defined at the resistance at room temperature divided by the saturated minimum in resistance at low temperature before the onset of superconductivity. $RRR(t)$ broadly divides into two regimes: for $t < 50$ nm, RRR is low (<30) with metallic transport down to 300 mK (highlighted in red); for $t > 50$ nm, RRR rapidly increases with increasing t with superconducting transport at low temperature (highlighted in blue). The low $RRR(t)$ values in the metallic regime cannot be simply explained on the basis of a thin-film effect or t approaching the out-of-plane superconducting coherence length of SRO_{214} which we estimate to be $\xi_c \sim 3$–8 nm (see Fig. 2c and Supplementary Note 2). The metallic regime indicates a large density of defects due to impurity phases in conjunction with structural defects (e.g. mosaic tilt or mosaic twist), consistent with the high (low) values of residual resistivity (ρ_0) for the films with a low (high) RRR as shown in Fig. 2d. In the superconducting regime, RRR reaches 110 for $t = 100$ nm, which is high relative to equivalently-thick SRO_{214} films reported elsewhere (Supplementary Fig. 6b).

Analysis of the microstructure. To identify the underlying mechanisms which suppress superconducting behavior in SRO_{214} films, we have systematically investigated the potential presence of structural defects that may affect long-range crystal order. We first discuss scanning transmission electron microscopy (STEM), high resolution scanning transmission electron microscopy (HR-STEM) and energy-dispersive X-ray (EDX) maps acquired on a SRO_{214} superconducting film (Fig. 3a–f) and a metallic film (Fig. 3g–l) (see Methods). We compare STEM (Fig. 3a, g) and HR-STEM micrographs which demonstrate coherent c-axis growth (Fig. 3b, l). For those films that show a full superconducting transition, the micrographs reveal inclusions near the SRO_{214}/LSAT interface (Fig. 3a). These crystalline (Fig. 3f) inclusions are elemental Ru (Fig. 3c–e) or Ru oxide (Supplementary Fig. 7) and spaced over distances larger than ξ_{ab} and so should not directly affect T_c.

For the SRO_{214} films that do not show a full superconducting transition, STEM maps consistently reveal a 1–2-nm-thick region above LSAT (indicated with an arrow) that has mixed stoichiometry (Fig. 3g). STEM-EDX confirms that this region has the correct Sr atomic concentration for SRO_{214}, but is deficient in Ru and rich in O (Fig. 3i–k). This is further confirmed by HR-STEM on different areas of the film (Fig. 3h,l), which show atomic layers of decreased concentration of heavy atoms, and stoichiometric SRO_{214} layers above and below this region (Fig. 3g)
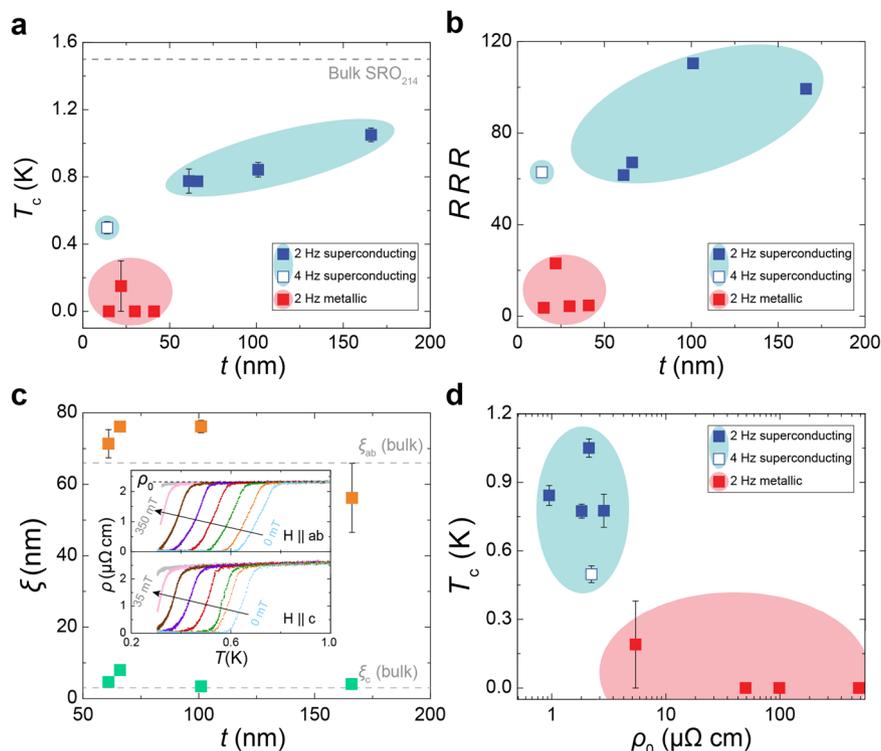
Fig. 2 Electronic transport properties of Sr$_2$RuO$_4$ films. a, b Thickness (t) dependence of the critical temperature T_c (**a**) and residual resistivity ratio *RRR* (**b**). Filled squares correspond to films grown with a laser frequency of 2 Hz and the hollow square at 4 Hz. **c** Superconducting coherence length in-plane ξ_{ab} (orange squares) and out-of-plane ξ_c (green squares) for multiple films versus t, determined from resistivity versus temperature measurements with a magnetic field applied along the ab-plane or the c-axis directions, respectively. **d** T_c versus residual resistivity ρ_0 for superconducting and metallic films marked as in (**a**) and (**b**). In all plots, background shading indicates a full superconducting transition (blue) or metallic (red) behaviour at low temperatures with or without incipient superconductivity.

(similar case observed in[33]). This depleted region most likely forms due to a separation of the Ruddlesden-Popper phase of SRO$_{214}$ into layers of SRO$_{113}$ or SRO$_{327}$ [34] (ferromagnetic and paramagnetic, respectively, with a perovskite structure), and SrO (rock salt unit cell). In the oxidizing atmosphere used during growth, SrO can stabilize into SrO$_2$ leading to O-rich and Ru-deficient regions matching the results extracted from EDX at the interface.

We note that SRO$_{113}$ and SRO$_{327}$ impurities are an issue for SRO$_{214}$ single crystals since the ferromagnetic exchange field of these phases can suppress superconductivity[26]. To investigate the presence of SRO$_{113}$ as well as SRO$_{327}$, we have measured the temperature dependence of the magnetic moment $m(T)$ of the non-superconducting SRO$_{214}$ films (Supplementary Fig. 8). We compare these data to a control sample of bare LSAT that has been exposed to matching conditions as SRO$_{214}$/LSAT films during growth but without SRO$_{214}$ deposited on the LSAT. $m(T)$ shows no evidence for SRO$_{113}$ since no ferromagnetic transition[35] is observed at or below the expected Curie temperature of 160 K or a maximum at 16 K due to SRO$_{327}$ (Supplementary Fig. 8a). We also investigated magnetization hysteresis loops $m(H)$ at a range of temperatures (20–300 K) with the applied field (H) directed normal to the LSAT substrate. For all T investigated, m is constant and matches the moment of bare LSAT within an error of 1 µemu (Supplementary Fig. 8a inset and 8b). This rules out the presence of ferromagnetic SRO$_{113}$ and would explain the XRD peak marked as "*" in Fig. 1c corresponding to SRO$_{327}$. Nevertheless the SRO$_{327}$ is not consistently observed and its presence/absence does not correlate with superconductivity. The possible SRO$_{327}$ phase would be concentrated at the

SRO$_{214}$/LSAT interface in the initial growth, considering the thickness dependence of our superconducting films. Such inter-growth could be controlled later by changing the dynamic nature of PLD. Further studies are highly desirable. Additionally, since STEM-EDX confirms stoichiometric Ru content[36] on the SRO$_{214}$ thin films (see example in Supplementary Fig. 2b), our study focuses on the analysis of structural defects that could alter the superconducting transition.

Degree of tilt and twist. Another potential source of crystal-lographic defects that may suppress superconductivity relate to misoriented crystalline regions. This can be visualized with the mosaic crystal model, in which the film is described as the combination of smaller crystallites (blocks), misoriented with respect to each other and the substrate. A rotation of these blocks about an axis parallel to the surface is known as mosaic tilt, and a rotation about an axis perpendicular to the surface is known as mosaic twist. Tilted and twisted blocks are separated by low-angle grain boundaries consisting of dislocations, which can be edge- or screw-like, with a Burgers vector (***b***) perpendicular or parallel to the dislocation line vector (***u***), respectively (see Supplementary Fig. 9), and cause local variations of interplanar distance (microstrain) at grain boundaries. Tilt can be measured from the full width half maximum in omega (FWHM$_\omega$) of the (0 0 l) dif-fracting planes by X-ray diffraction in a symmetric (coplanar) geometry. Values of tilt extracted from SRO$_{214}$ films with dif-ferent t show that all films (superconducting or non-super-conducting), with the exception of one, have similar values of tilt. Tilt does not therefore affect the electrical properties SRO$_{214}$ films (see Supplementary Fig. 10a–c).
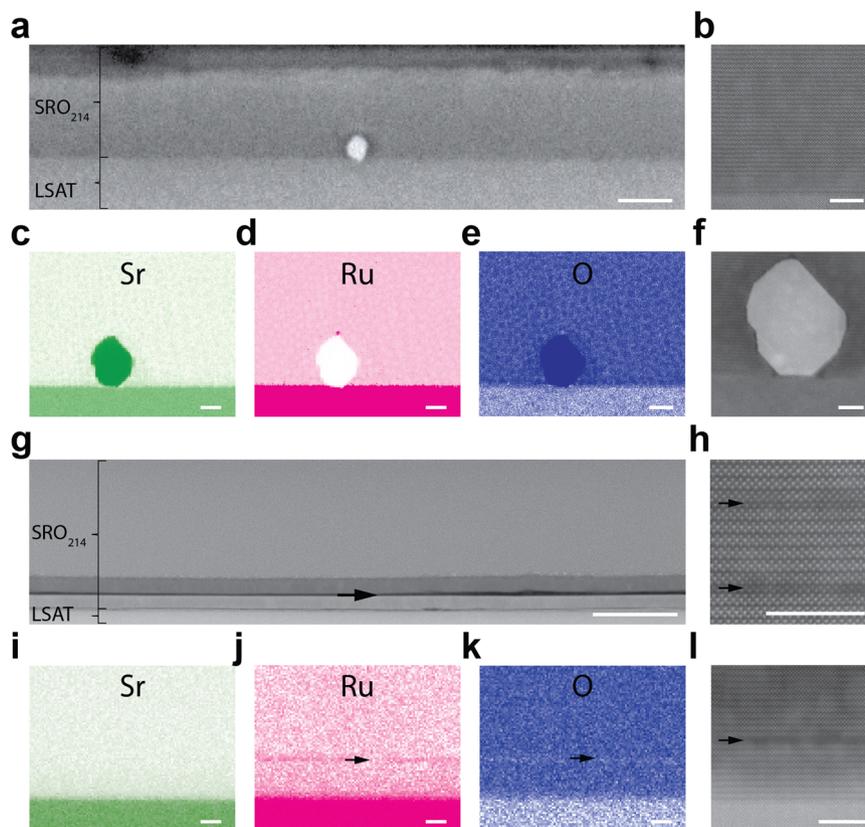
Fig. 3 Structural and chemical properties of Sr$_2$RuO$_4$ films. a–f Scanning transmission electron microscopy STEM micrographs of a superconducting film of a thickness $t = 66$ nm (**a**) showing inclusions at the Sr$_2$RuO$_4$/(La$_{0.3}$Sr$_{0.7}$)(Al$_{0.65}$Ta$_{0.35}$)O$_3$ (LSAT) interface and high resolution HR-STEM of an area close to the same interface in (**b**). EDX maps of the inclusions in **a** are shown in **c-e** for Sr (**c**), Ru (**d**) and O (**e**) with a HR-STEM micrograph of the inclusion in **f**. **g–l** STEM micrograph of a $t = 41$ nm metallic film (**g**) showing an interface layer of different stoichiometry (dark black line indicated with an arrow) to the rest of the film with corresponding energy-dispersive X-ray EDX maps for Sr (**i**), Ru (**j**) and O (**k**). **h, l** HR-STEM on an area of the Sr$_2$RuO$_4$ thin film (**h**) and Sr$_2$RuO$_4$/(La$_{0.3}$Sr$_{0.7}$)(Al$_{0.65}$Ta$_{0.35}$)O$_3$ interface (**l**) showing a decreased concentration of heavy atoms in some of the layers. **g–l** Depleted region indicated with arrows. The scale bars are **a**, 50 nm, **b, f, h, l** 5 nm, **c, d, e, l, j, k** 10 nm and **g**, 25 nm. Note that in (**c-e**) and (**i-k**), bright regions indicate higher atomic percent. The subindex 214 refers to Sr$_2$RuO$_4$ and LSAT corresponds to the substrate (La$_{0.3}$Sr$_{0.7}$)(Al$_{0.65}$Ta$_{0.35}$)O$_3$.

Twist can be measured using four different configurations: edge [by measuring the $(h\,k\,0)$ planes from the FWHM$_\omega$ with an offset in chi (χ_{offset}) of 90° (Fig. 4a)]; glancing angle in-plane; transmission; or skew geometry[37]. For our thin-film geometry we adopt the skew geometry (non-coplanar) configuration because the signal intensity is the strongest, and measure the FWHM$_\omega$ of the $(4\,1\,3)$ diffracting planes, which provides a good estimate of twist due to the large χ_{offset} (>70°)[37,38]. The dependence of twist, FWHM$_\omega$ extracted from a pseudo-Voigt profile fit after the subtraction of the instrumental contribution (see Supplementary Note 3), on t is shown on Fig. 4a. Since the in-plane crystallite size ($L_{||}$) is of the order of micrometres, its contribution to peak broadening is negligible (see Supplementary Fig. 10a). We observe that FWHM$_\omega$ (Fig. 4b inset), and hence the degree of twist, rapidly rises as t decreases below 50 nm, corresponding to the metallic films that do not show full superconducting transition (Fig. 4b). From Fig. 4c we demonstrate a direct correlation between twist and the suppression of superconductivity by a reduction (increase) of T_c (residual resistivity) when the degree of twist increases.

Identification of dislocations. The increase in twist with decreasing t (Fig. 4b) indicates a higher concentration of dislocations with b in-plane at low t for non-superconducting films. To confirm this and determine the nature of the dislocations, we have performed $g \cdot b$ TEM analysis, with g being the diffracted

beam direction on a superconducting and non-superconducting film. In $g \cdot b$ TEM analysis, dislocations are in-contrast (visible) when $g \cdot b \neq 0$, but out-of-contrast (invisible) for $g \cdot b = 0$[39,40] as illustrated in Fig. 4a. Figure 4d–o shows $g \cdot b$ bright field TEM analysis performed on three different cross-sectional areas for the superconducting and non-superconducting films using two perpendicular diffraction vectors g_{00l} and g_{h00}. The non-superconducting films shows a larger concentration of dislocations compared to the superconducting film. Furthermore, for the non-superconducting film the dislocations are mostly in-plane and screw-like with both u and b in- plane (horizontal orange arrow), as they can only be resolved when $b \parallel g_{h00}$ (Fig. 4d–f) and are extinct when $b \perp g_{00l}$ (Fig. 4g–i). These results are consistent with the high degree of twist observed in non-superconducting films and therefore demonstrate that horizontal screw dislocations are a key defect that strongly suppresses superconductivity in SRO$_{214}$. In contrast, the lower density of dislocations present in the superconducting film are in-plane edge-like with u in-plane and b out-of-plane (vertical orange arrow), as they are visible when $b \parallel g_{00l}$ (Fig. 4j–l) and not visible when $b \perp g_{h00}$ (Fig. 4m–o). In both the superconducting and non-superconducting films, a few threading mixed dislocations, with both edge and screw components (tilted orange arrow) are resolved with both g_{00l} and g_{h00}. The presence of threading dislocations with a screw component is also revealed in topographic images acquired using an atomic force microscope (Supplementary Fig. 10d–g).
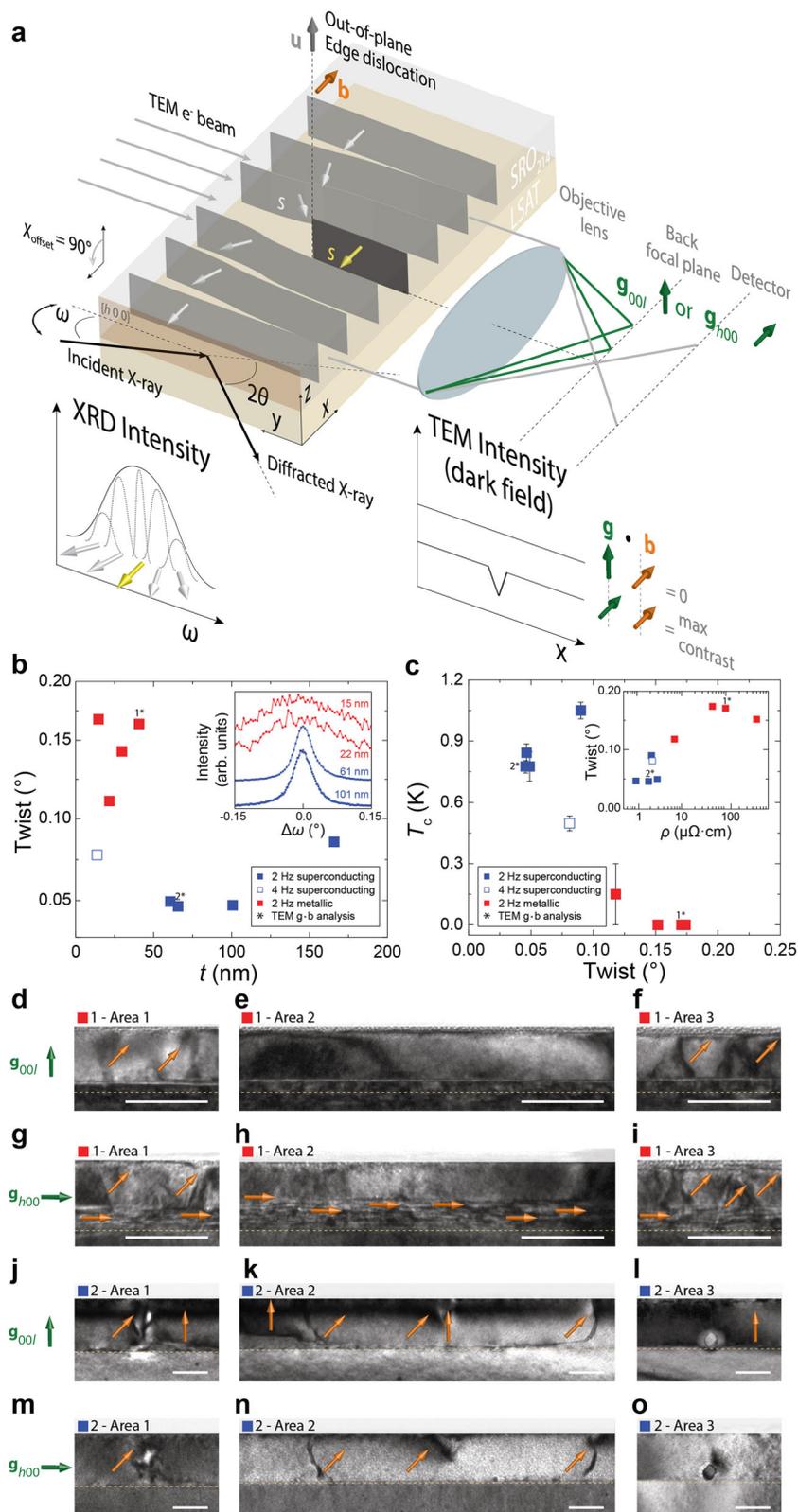
We note that, we cannot confirm that the white contrast in Fig. 3j located in the Ru-deficient layer (confirmed in Fig. 4g–i), is also dislocation related as it might be the result of a combination of features such as Ru-deficiency, interface effect and dislocations.

Finally, we note that the superconductivity in SRO_{214} can be further optimized by tuning additional growth parameters (not discussed in this paper) such as deposition frequency. We have tested the effect of doubling the laser pulse frequency to 4 Hz during SRO_{214} growth, while keeping the same growth conditions as for the rest of the study (oxygen pressure of 0.35 Pa, fluence of 1.0 J cm^{-2}, 950 ℃), which has the effect of reducing the degree of twist (Fig. 4b) and the residual resistivity (Fig. 2d), and increasing T_c (Fig. 3a) and RRR (Fig. 3b), compared to equivalent films grown at 2 Hz.

Fig. 4 Nature of dislocations and their effect on superconductivity in Sr$_2$RuO$_4$ films. a An illustration of an edge dislocation with an out-of-plane line vector $\boldsymbol{u}$ (grey arrow) and Burgers vector $\boldsymbol{b}$ in-plane (orange arrow) on the $(h\,0\,0)$ planes of SRO$_{214}$. The diagram also shows the X-ray diffraction setup in edge geometry (Tilt angle of the sample stage $\chi_{offset} = 90°$) to measure the in-plane misorientation, twist, from the peak broadening in ω (angle between the X-ray incident beam and the diffracted planes) due to variations in the scattering direction (white and yellow arrows). Transmission electron microscopy TEM $\boldsymbol{g} \cdot \boldsymbol{b}$ analysis to reveal edge dislocations using bright field imaging with two perpendicular diffraction conditions ($\boldsymbol{g}_{00l}$ and $\boldsymbol{g}_{h00}$) is also shown. **b** Degree of twist versus thin-film thickness t, determined from the full width half maximum in ω FWHM$_\omega$, measured from $\chi_{offset} \sim 78°$ in skew symmetric on the $(4\,1\,3)$ planes (inset curves are vertically offset for clarity). **c**, Superconducting critical temperature T_c versus and resistivity ρ versus twist (inset). **d–o** $\boldsymbol{g} \cdot \boldsymbol{b}$ analysis by bright field TEM showing dislocations on three areas of a lamella from metallic (**d-i**) and superconducting (**j-o**) SRO$_{214}$ films (marked as three asterisks in **b** and **c**). The diffraction vectors $\boldsymbol{g}_{00l}$ and $\boldsymbol{g}_{h00}$ are indicated by green arrows and $\boldsymbol{b}$ by orange arrows: for in-plane edge dislocations the arrows are horizontal, for out-of-plane screw dislocations the arrows are vertical, and for mixed dislocation the arrows are tilted. The interface film/substrate interface is marked with a yellow dotted line. Scale bar in **d-o**, 50 nm.

Discussion

In conclusion, we have systematically investigated the structure-electrical-properties relationship of SRO$_{214}$ thin-films grown on LSAT by pulsed laser deposition from a single crystal SRO$_{327}$ target. The absence of superconductivity in films thinner than 50 nm is correlated with the in-plane misorientation mosaic twist, caused by in-plane screw dislocations, and with the most defective region near the SRO$_{214}$/LSAT interface. The application of single crystal SRO$_{327}$ targets offers a robust reliable platform for the creation of superconducting SRO$_{214}$ thin-films and will initiate experimental studies involving multilayer structures and devices based on this highly important superconducting oxide.

Methods

Substrate preparation and growth. SRO$_{214}$ films are grown by pulsed laser deposition onto $5 \times 5 \times 0.5$ mm^3 single crystal $(0\,0\,1)$ (LaAlO$_3$)$_{0.3}$-(Sr$_2$AlTaO$_6$)$_{0.7}$ (LSAT) with miscut angles of less than 0.05°. Prior to loading into the pulsed laser deposition chamber, the LSAT substrates are ultrasonicated for 10 min in acetone followed by 10 min in isopropyl, and subsequently dried using nitrogen gas. The LSAT substrates are attached to a SiC crystal (10×10 mm^2) with Pt paste (Tanaka Kikinzoku Kogyo K.K.) and secured with clips onto the substrate holder. The LSAT substrates are pre-baked for 30 min at 250°C in vacuum in the load-lock chamber. In the main chamber, the LSAT is annealed in ultra-high vacuum (7.5e-6 Pa) for 30 min at 950°C to promote terrace formation, with a warming ramp rate of 50 °C min^{-1}. The SRO$_{214}$ films are grown in different oxygen pressures and KrF excimer laser (LPXpro 210 F Coherent Inc. 248 nm) energies as discussed in the main paper with the LSAT substrate temperature maintained at 950°C using an infrared diode laser heater. The SRO$_{214}$ films are deposited by ablating from a single crystal target of SRO$_{327}$ at a repetition rate of 2 Hz for the majority of the samples prepared in this work (or 4 Hz for one film) and a substrate to target distance of 5 cm. Following film growth, the sample is cooled in oxygen at a rate of 50°C min^{-1}.

Target preparation. Single crystal targets of SRO$_{327}$ are prepared by floating zone method as discussed in refs. [41,42]. These are cleaved in isopropyl and ultrasonicated for 10 min in acetone and then 10 min in isopropanol and subsequently dried using nitrogen gas. The cleaved crystals have a volume of approximately $3 \times 10 \times 0.5$ mm^3. The surfaces of the crystals are examined by optical microscopy with polarized light to confirm a low concentration of Ru and SRO$_{113}$ surface impurities. The SRO$_{327}$ target is attached to a holder (polycrystalline SRO$_{214}$) using Epoxy-Ag paste and cured for 30 min at 150°C. Prior to loading it into the pulsed laser deposition main chamber, the SRO$_{327}$ target is baked for 30 min at 250°C in vacuum in the load-lock.

Transport and magnetic measurements. Electrical transport measurements are performed in a pulsed tube cryogen free physical property measurement system. Electrical resistance is measured using a current-bias four-point electrical setup with Au contact pads evaporated onto the SRO$_{214}$ surface.

X-ray diffraction. X-ray diffraction data were acquired using a Panalytical Empyrean X-ray diffractometer, with a Cu$_{K\alpha1}$ X-ray source and a hybrid two bounce primary monochromator.

Transmission electron microscopy. Samples for transmission electron microscopy are prepared using focused ion beam milling. Bright field transmission electron microscopy imaging for $g \cdot b$ analysis is performed using an FEI Tecnai Osiris at 200 kV. Compositional mapping is carried out using scanning transmission electron microscopy (STEM) – energy dispersed X-ray spectroscopy (EDX) in the same instrument, employing a Super-X detector with a total collection solid angle of 0.9 sr. High resolution STEM images are acquired on a probe-corrected FEI Titan operated at 300 kV.

Data availability

Supporting research data have been deposited in the University of Cambridge research repository and it is publicly available at https://doi.org/10.17863/CAM.48463.

References

1. Linder, J. & Robinson, J. W. A. Superconducting spintronics. *Nat. Phys.* **11**, 307–315 (2015).
2. Robinson, J. W. A., Witt, J. D. S. & Blamire, M. G. Controlled injection of spin-triplet supercurrents into a strong ferromagnet. *Science.* **329**, 59–61 (2010).
3. Khaire, T. S., Khasawneh, M. A., Pratt, W. P. & Birge, N. O. Observation of spin-triplet superconductivity in co-based josephson junctions. *Phys. Rev. Lett.* **104**, 137002 (2010).
4. Shibuya, K., Mi, S., Jia, C.-L., Meuffels, P. & Dittmann, R. Sr$_2$TiO$_4$ layered perovskite thin films grown by pulsed laser deposition. *Appl. Phys. Lett.* **92**, 241918 (2008).
5. Anwar, M. S., Veldhorst, M., Brinkman, A. & Aarts, J. Long range supercurrents in ferromagnetic CrO$_2$ using a multilayer contact structure. *Appl. Phys. Lett.* **100**, 052602 (2012).
6. Gingrich, E. C. et al. Spin-triplet supercurrent in Co/Ni multilayer Josephson junctions with perpendicular anisotropy. *Phys. Rev. B* **86**, 224506 (2012).
7. Di Bernardo, A. et al. Signature of magnetic-dependent gapless odd frequency states at superconductor/ferromagnet interfaces. *Nat. Commun.* **6**, 8053 (2015).
8. Di Bernardo, A. et al. Intrinsic paramagnetic Meissner effect due to s-wave odd-frequency superconductivity. *Phys. Rev. X* **5**, 041021 (2015).
9. Srivastava, A. et al. Magnetization control and transfer of spin-polarized cooper pairs into a half-metal manganite. *Phys. Rev. Appl.* **8**, 044008 (2017).
10. Jeon, K.-R. et al. Enhanced spin pumping into superconductors provides evidence for superconducting pure spin currents. *Nat. Mater.* **17**, 499–503 (2018).
11. Xu, H. Signatures of majorana fermions in topological superconductor nanowires. in *Extended Abstracts of the 2014 International Conference on Solid State Devices and Materials* (The Japan Society of Applied Physics, 2014).
12. Bommer, J. D. S. et al. Spin-orbit protection of induced superconductivity in majorana nanowires. *Phys. Rev. Lett.* **122**, 187702 (2019).
13. Wei, P., Manna, S., Eich, M., Lee, P. & Moodera, J. Superconductivity in the surface state of noble metal gold and its fermi level tuning by EuS dielectric. *Phys. Rev. Lett.* **122**, 247002 (2019).
14. Maeno, Y. et al. Superconductivity in a layered perovskite without copper. *Nature* **372**, 532–534 (1994).
15. Mackenzie, A. P., Scaffidi, T., Hicks, C. W. & Maeno, Y. Even odder after twenty-three years: the superconducting order parameter puzzle of Sr$_2$RuO$_4$. *npj Quantum Mater.* **2**, 40 (2017).
16. Barber, M. E., Gibbs, A. S., Maeno, Y., Mackenzie, A. P. & Hicks, C. W. Resistivity in the vicinity of a van Hove singularity: Sr$_2$RuO$_4$ under uniaxial pressure. *Phys. Rev. Lett.* **120**, 76602 (2018).
17. Kallin, C. Chiral p-wave order in Sr$_2$RuO$_4$. *Reports Prog. Phys.* **75**, 042501 (2012).
18. Luke, G. M. et al. Time-reversal symmetry breaking superconductivity in Sr$_2$RuO$_4$. *Nature* **394**, 558–561 (1998).
19. Xia, J., Maeno, Y., Beyersdorf, P. T., Fejer, M. M. & Kapitulnik, A. High resolution polar Kerr effect measurements of Sr$_2$RuO$_4$: evidence for broken

20. Ishida, K. et al. Spin-triplet superconductivity in Sr_2RuO_4 identified by ^{17}O Knight Shift. *Nature* **396**, 658–660 (1998).
21. Murakawa, H., Ishida, K., Kitagawa, K., Mao, Z. Q. & Maeno, Y. Measurement of the ^{101}Ru -knight shift of superconducting Sr_2RuO_4 in a parallel magnetic field. *Phys. Rev. Lett.* **93**, 167004 (2004).
22. Duffy, J. A. et al. Polarized-neutron scattering study of the cooper-pair moment in Sr_2RuO_4. *Phys. Rev. Lett.* **85**, 5412–5415 (2000).
23. Pustogow, A. et al. Constraints on the superconducting order parameter in Sr_2RuO_4 from oxygen-17 nuclear magnetic resonance. *Nature* **574**, 72–75 (2019).
24. Schlom, D. & Jia, Y. Searching for superconductivity in epitaxial films of copper-free layered oxides with the K_2NiF_4 structure. *Proc. SPIE* **3481**, 226–240 (1998).
25. Mackenzie, A. P. et al. Extremely strong dependence of superconductivity on disorder in Sr_2RuO_4. *Phys. Rev. Lett.* **80**, 161–164 (1998).
26. Kikugawa, N., Mackenzie, A. P. & Maeno, Y. Effects of in-plane impurity substitution in Sr_2RuO_4. *Phys. Soc. Jpn* **72**, 237–240 (2003).
27. Marshall, P. B., Kim, H., Ahadi, K. & Stemmer, S. Growth of strontium ruthenate films by hybrid molecular beam epitaxy. *APL Mater.* **5**, 096101 (2017).
28. Krockenberger, Y. et al. Growth of superconducting Sr_2RuO_4 thin films. *Appl. Phys. Lett.* **97**, 082502 (2010).
29. Cao, J. et al. Enhanced localized superconductivity in Sr_2RuO_4 thin film by pulsed laser deposition. *Supercond. Sci. Technol.* **29**, 095005 (2016).
30. Uchida, M. et al. Molecular beam epitaxy growth of superconducting Sr_2RuO_4 films. *APL Mater.* **5**, 106108 (2017).
31. Nair, H. P. et al. Demystifying the growth of superconducting Sr_2RuO_4 thin films. *APL Mater.* **6**, 101108 (2018).
32. Ohnishi, T. & Takada, K. Epitaxial thin-film growth of $SrRuO_3$, $Sr_3Ru_2O_7$, and Sr_2RuO_4 from a $SrRuO_3$ target by pulsed laser deposition. *Appl. Phys. Express* **4**, 025501 (2011).
33. Marshall, P. B., Ahadi, K., Kim, H. & Stemmer, S. Electron nematic fluid in a strained $Sr_3Ru_2O_7$ film. *Phys. Rev. B* **97**, 155160 (2018).
34. Ikeda, S.-I., Maeno, Y., Nakatsuji, S., Kosaka, M. & Uwatoko, Y. Ground state in $Sr_3Ru_2O_7$: Fermi liquid close to a ferromagnetic instability. *Phys. Rev. B* **62**, R6089–R6092 (2000).
35. Xia, J., Siemons, W., Koster, G., Beasley, M. R. & Kapitulnik, A. Critical thickness for itinerant ferromagnetism in ultrathin films of $SrRuO_3$. *Phys. Rev. B* **79**, 140407 (2009).
36. Kim, G. et al. Electronic and vibrational signatures of ruthenium vacancies in $Sr2RuO4$ thin films. *Phys. Rev. Mater.* **3**, 094802 (2019).
37. Moram, M. A. & Vickers, M. E. X-ray diffraction of III-nitrides. *Reports Prog. Phys.* **72**, 036502 (2009).
38. Lee, S. R. et al. Effect of threading dislocations on the Bragg peakwidths of GaN, AlGaN, and AlN heterolayers. *Appl. Phys. Lett.* **86**, 241904 (2005).
39. Williams, D. B. & Carter, C. B. *Transmission electron microscopy: a textbook for materials science*. (Springer, 2009).
40. Massabuau, F. C.-P., Bruckbauer, J., Trager-Cowan, C. & Oliver, R. A. *Characterisation and Control of Defects in Semiconductors*. (The Institution of Engineering and Technology, London, 2019).
41. Perry, R. S. & Maeno, Y. Systematic approach to the growth of high-quality single crystals of $Sr_3Ru_2O_7$. *J. Cryst. Growth* **271**, 134–141 (2004).
42. Maeno, Y. et al. Enhancement of Superconductivity of Sr_2RuO_4 to 3 K by Embedded Metallic Microdomains. *Phys. Rev. Lett.* **81**, 3765 (1998).

Author contributions
J.W.A.R. devised the original project and developed it with C.M.P.G. alongside T.W.N., Y.M. C.M.P.G. and J.W.A.R. analysed the data with support from A.D.B., G.K., A.V., Y.M. and T.W.N. Thin-films were fabricated by C.M.P.G. with support from A.D.B., H.G.L., S.K., J.K., B.K. and Y.Y. Electrical and magnetic properties were characterised by C.M.P.G. with the support of A.D.B., S.K. and G.K. Microstructural properties were characterised by X-ray diffraction by C.M.P.G. with support from M.E.V. and input from G.K. Transmission electron microscopy was performed by F.C-P.M and G.D. $Sr_3Ru_2O_7$ crystals were fabricated by Y.M. as well as by R.F. along with A.V. M.G.B. provided input into the growth of the thin films. All authors commented on the paper. C.M.P.G. and J.W.A.R. wrote the manuscript with input from A.D.B., G.K., S.K., M.E.V. and F.C-P.M.

Competing interests
The authors declare no competing interests.

Additional information
Supplementary information is available for this paper at https://doi.org/10.1038/s43246-020-0026-1.

Correspondence and requests for materials should be addressed to J.W.A.R.

Reprints and permission information is available at http://www.nature.com/reprints

Publisher's note Springer Nature remains neutral with regard to jurisdictional claims in published maps and institutional affiliations.